Climate
of the Past

Transitivity of the climate–vegetation system in a warm climate

U. Port[1] and M. Claussen[1,2]

[1]Max Planck Institute for Meteorology, 20146 Hamburg, Germany
[2]Meteorological Institute, University of Hamburg, 20146 Hamburg, Germany

Correspondence to: U. Port (ulrike.port@mpimet.mpg.de)

Abstract. To date, the transitivity of the global system has been analysed for late Quaternary (glacial, interglacial, and present-day) climate. Here, we extend this analysis to a warm, almost ice-free climate with a different configuration of continents. We use the Earth system model of the Max Planck Institute for Meteorology to analyse the stability of the climate system under early Eocene and pre-industrial conditions. We initialize the simulations by prescribing either dense forests or bare deserts on all continents. Starting with desert continents, an extended desert remains in central Asia in the early Eocene climate. Starting with dense forest coverage, the Asian desert is much smaller, while coastal deserts develop in the Americas which appear to be larger than in the simulations with initially bare continents. These differences can be attributed to differences in the large-scale tropical circulation. With initially forested continents, a stronger dipole in the 200 hPa velocity potential develops than in the simulation with initially bare continents. This difference prevails when vegetation is allowed to adjust to and interact with climate. Further simulations with initial surface conditions that differ in the region of the Asian desert only indicate that local feedback processes are less important in the development of multiple states. In the interglacial, pre-industrial climate, multiple states develop only in the Sahel region. There, local climate–vegetation interaction seems to dominate.

1 Introduction

The interaction between atmosphere and vegetation may allow for multiple equilibria of the system, pointing to intransitive dynamics in the climate system as suggested by Lorenz (1968). Multiple equilibrium states have been detected in various model simulations when initialized with different vegetation covers. Claussen (1994), Claussen and Gayler (1997), Claussen (1998), Kubatzki and Claussen (1998), Wang and Eltahir (2000), Zeng and Neelin (2000), and Rachmayani et al. (2015) found multiple states in northern Africa; Oyama and Nobre (2003) found these in the Amazon region, Claussen (1998) in central Asia, and Dekker et al. (2010) found them in the northern high latitudes. In all cases, simulations with initially more extended vegetation cover lead to a moister climate and smaller deserts than simulations initialized with sparse vegetation coverage.

Studies which focus on palaeoclimates indicate that the stability of the climate–vegetation system depends on the climate state. For example, the intransitivity of the climate–vegetation system over northern Africa vanishes, or becomes much less pronounced, for the mid-Holocene climate in the simulations by Claussen and Gayler (1997) and Rachmayani et al. (2015). Likewise, Bathiany et al. (2012) showed that the pattern of bistability over northern Africa changes at different times in different locations during the transition from mid- to late Holocene. Such changes in the stability of the climate–vegetation system may lead to abrupt changes in vegetation and climate due to a loss of stability in the regions which exhibit multiple states (Brovkin et al., 1998; Claussen et al., 1999; Renssen et al., 2003). Further, changes in the stability of the climate–vegetation system may even induce abrupt changes in locations which seem to be more stable but which are interlinked with the unstable locations (Bathiany et al., 2013a, b).

To date, most studies have assessed the stability of the climate–vegetation system for interglacial or glacial climate, i.e. for climate states with permanent ice sheets. Little is known about the transitivity of the climate–vegetation system in climates that differ strongly from the current late Quaternary climate. Therefore, we explore the stability of the

climate–vegetation system in a much warmer climate than the present one, which does not support permanent ice sheets and sea ice.

During the early Eocene (about 54 to 52 Myr ago) such a warm, almost ice-free climate prevailed. An atmospheric CO_2 concentration between 300 and 2000 ppm (Beerling and Royer, 2011) as well as the specific distribution of continents and bathymetry led to 5 to 6 °C warmer tropics (Pearson et al., 2007) and to mostly ice-free poles (Zachos et al., 1992). The warm climate allowed a dense vegetation cover in almost all regions (Willis and McElwain, 2002). Even on Antarctica and in the high north, flora fossils indicate a dense tree cover (Wolfe, 1985; Eberle and Greenwood, 2012; Harrington et al., 2012; Pross et al., 2012).

We perform simulations with the Earth system model of the Max Planck Institute for Meteorology (MPI-ESM) and assume continents, bathymetry, and atmospheric CO_2 concentration according to the early Eocene. Other boundary conditions such as orbital parameters, atmospheric methane, and nitrous oxide as well as the assumed plant species in the dynamic vegetation module are the same as in pre-industrial simulations. The resulting simulated climate matches temperature reconstructions of the early Eocene fairly well. Only in the high latitudes is the simulated near-surface temperature lower than reconstructions suggest. Despite this mismatch, the simulated Eocene-like climate meets our specifications because we aim to investigate the stability of the climate–vegetation system in a warm, almost ice-free climate rather than to reproduce the climate of the early Eocene as accurately as possible.

To compare the stability of the climate–vegetation system in the warm Eocene-like climate and in the pre-industrial climate, we perform the same experiment with boundary conditions for both these climates. The respective experiments contain two simulations each which start from different vegetation states: all ice-free continents are either completely covered with dense forests or with bare-soil deserts. From these initial states, the model system is allowed to freely evolve, with dynamically interacting atmosphere, ocean, and vegetation. Depending on the initial conditions, new equilibria in the climate–vegetation system are reached after some 1000 years of simulation.

2 Experiment

2.1 Model

The Earth system model of the Max Planck Institute for Meteorology (MPI-ESM) consists of the atmospheric general circulation model ECHAM6 (Stevens et al., 2013), the Max Planck Institute Ocean Model MPIOM (Jungclaus et al., 2013), the land surface scheme JSBACH (Reick et al., 2013), and the ocean biogeochemistry model HAMOCC (Ilyina et al., 2013). We use ECHAM6 in a horizontal resolution of T31 (approximately 3.75°) and with 31 levels in the vertical.

Table 1. List of plant functional types (PFTs) defined in the land surface scheme JSBACH.

Plant functional type
Tropical evergreen trees
Tropical deciduous trees
Extra-tropical evergreen trees
Extra-tropical deciduous trees
Raingreen shrubs
Cold shrubs
C_3 grass
C_4 grass

Table 2. Boundary conditions in the early Eocene climate simulations and in the pre-industrial climate simulations.

	Pre-industrial	Early Eocene
CO_2 concentration	280 ppm	560 ppm
Methane	0.8 ppm	0.8 ppm
Nitrous oxide	0.288 ppm	0.288 ppm
Orbit	pre-industrial	pre-industrial
Bathymetry and orography	present-day	Bice and Marotzke (2001)
Ice sheets	pre-industrial	none

The ocean grid has a horizontal resolution of about 3° and 40 levels in depth. JSBACH includes a dynamic vegetation module based on a tiling approach (Brovkin et al., 2009). Vegetation is represented by eight plant functional types (PFTs) which reflect present-day plant taxa (Table 1).

We perform the same simulations for an interglacial climate and a warm ice-free climate. To get an interglacial climate, we assume pre-industrial boundary conditions for the chemical composition of the atmosphere, orbital parameters, continents, orography, and bathymetry (Table 3). To achieve a warm ice-free climate, we use the boundary conditions which Heinemann et al. (2009) use for their Eocene simulation. Like them, we prescribe the orography and bathymetry maps by Bice and Marotzke (2001). The orography map lacks information on sub-grid orography such as slope, anisotropy, orientation, standard deviation, maximum, minimum, and mean elevation. Without this information, sub-grid interactions of atmospheric flow with orography can not be parameterized in ECHAM6 (Stevens et al., 2013). Hence, we turn off the module for sub-grid orographic drag and wave generation.

In the standard version of MPIOM, the grid poles are over Greenland and Antarctica. With Eocene continents, the pole over present-day Greenland coincides with the palaeo-Atlantic Ocean, i.e. meridians converge at this pole leading to numerical singularities. To avoid singularities, we use the setting by Heinemann et al. (2009), who placed the MPIOM North Pole and South Pole in the large continents of palaeo-Asia and to palaeo-South America, respectively.

Table 3. Simulations included in the experiment.

	Initial state	Boundary conditions
FP_d	Forest world	Pre-industrial
DP_d	Desert world	Pre-industrial
FE_d	Forest world	Early Eocene
DE_d	Desert world	Early Eocene
DA_d	Forest world with desert in Asia	Early Eocene
FA_d	Desert world with forest in Asia	Early Eocene

The atmospheric CO_2 concentration is fixed to 560 ppm (Table 2), which is the lower limit of reconstructions (Zachos et al., 2001; Beerling and Royer, 2011). With a fixed atmospheric CO_2 concentration, carbon pools does not need to reach an equilibrium, which would take several thousand years. Instead, living biomass responds to a constant atmospheric CO_2 and equilibrates already after several decades. Since our simulations run for 1000 years, this time span is long enough to reach an equilibrium in living biomass.

The other greenhouse gases, methane and nitrous oxide, are set to pre-industrial values in the early Eocene atmosphere, and the orbit also corresponds to the pre-industrial orbit (Table 2). Soil properties are the same as in the pre-industrial simulations and represent clay. Soil dynamics are not considered, i.e. soils remain constant over all the simulations.

During the early Eocene, plant species differed from today. For instance, grass land is common today but evolved after the early Eocene (Willis and McElwain, 2002). C_3 spread in the early to mid-Miocene (20–10 Ma) (Janis, 1993), while C_4 expanded during the mid- to late Miocene (Cerling et al., 1993). Instead, other plant species dominated the vegetation cover during the early Eocene, which are extinct, or almost extinct, today, such as paratropical rainforest or polar forest (Wolfe, 1985). We neglect any differences in plant taxa to isolate the geographic and climatic factors affecting the stability of the climate–vegetation system.

To initialize our Eocene simulations, we perform a simulation starting from the equilibrium Eocene climate by Heinemann et al. (2009). Like their simulation, we assume a savannah vegetation with a desert cover of 40 %, a tree cover of 24 %, and a grass cover of 36 %. After 300 years, near-surface temperature and upper-level ocean temperatures are in equilibrium. Only in the deep ocean does a marginal temperature trend remain.

2.2 Simulations

Starting from the equilibrium Eocene climate, we perform two simulations. In the first 400 years of the simulations, vegetation is fixed to dense forest in the FE_f simulation and to bare soil in the DE_f simulation. After that period, the forest world and desert world simulation continue with a dynami-

cally evolving vegetation cover in the FE_d simulation and in the DE_d simulation, respectively.

In order to separate the albedo effect of vegetation from the hydrological effect, we perform the initial desert simulation and the initial forest simulation two times. All soils either have a homogeneous albedo of 0.1 (dark soil) or 0.4 (bright soil). In the dark-soil case, soil and vegetation have about the same albedo, leading to weak albedo changes by vegetation relative to bare soil. In other words, vegetation affects climate mainly through the hydrological cycle. In the bright-soil case, vegetation has a much lower albedo than soil. Hence, both the albedo effect and the hydrological effect of vegetation exist. In the bright-soil simulations, the climate–vegetation system reaches the same state when initialized with dense forest as when initialized with bare soil. As we focus on intransitive dynamics in the climate–vegetation system, we exclude a detailed discussion of the bright-soil simulations in this study. Instead, we present the results for the dark-soil simulations where multiple equilibria are established depending on the initial vegetation cover in the warm ice-free climate. Table 3 gives an overview of the four simulations considered where all soils have a low soil albedo.

To analyse the local impact of initial vegetation cover on the intransitivity, we perform two additional simulations with Eocene boundary conditions. In the DA_f simulation, we fix the vegetation cover to bare soil in central Asia and to forests elsewhere and simulate 400 years. Starting from the DA_f simulation, we let the vegetation evolve dynamically in the DA_d simulation. Analogously, we assume a dense forest in central Asia and deserts elsewhere in the FA_f simulation. After 400 years with a fixed vegetation cover, vegetation evolves dynamically in the FA_d simulation.

Analogously to the Eocene simulations, we perform two pre-industrial simulations. The FP_f simulation runs for 400 years with a fixed forest cover on all ice-free continents. Afterwards, vegetation establishes itself dynamically in the FP_d simulation. In the DP_f simulation, vegetation is fixed to desert for 400 years. Starting from the DP_f simulation, vegetation evolves dynamically in the DP_d simulation.

3 Warm, almost ice-free climate and its vegetation cover

Near-surface temperature in the DE_d simulation agrees with temperature reconstructions of the early Eocene temperature in the topics and subtropics. In the northern mid- to high latitudes, the DE_d simulation is colder than reconstructions of Eocene temperatures (Fig. 1). Relative to the TEX_{86} estimate by Sluijs et al. (2006) north of Greenland, the simulated sea-surface temperature (SST) is as much as 18 K lower. The TEX_{86} estimate, however, likely represents summer temperatures (Sluijs et al., 2006). Considering summer values, the
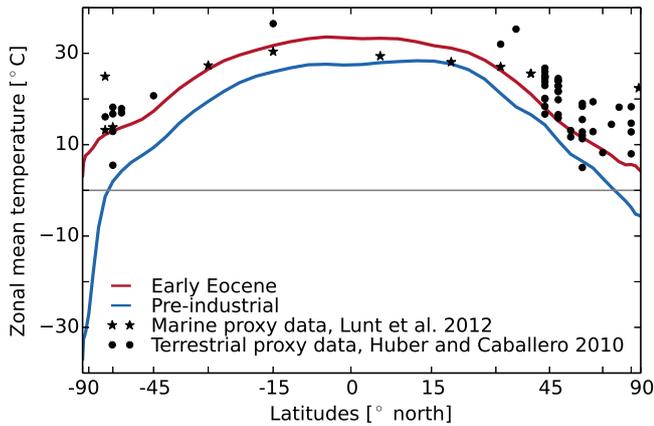
Figure 1. Zonal annual mean 2 m temperature in the DE_d simulation (red line) and in the DP_d simulation (blue line). Stars show estimates of annual mean sea-surface temperature (SST) and near-surface temperature for the early Eocene based on $\delta^{18}O$, Mg / Ca, and TEX$_{86}$ (Lunt et al., 2012). Cycles refer to terrestrial annual mean temperature estimates based on macrofloral and palynoflora assemblage data and from teeth, hydrogen isotopes, and oxygen isotopes (Huber and Caballero, 2011).

DE_d simulation is 15 K colder than temperature estimates suggest for the early Eocene.

In the southern high latitudes, the simulation agrees with marine and terrestrial temperature estimates. The only exception is the SST reconstruction by Bijl (2009), which suggest a temperature of 24 °C on the Tasman Plateau (Fig. 1). Like the estimate by Sluijs et al. (2006), the estimate by Bijl (2009) is based on TEX$_{86}$ and likely has a bias to summer temperatures. Considering the summer temperature, our simulation is colder than the reconstruction by 9 K over the southern Pacific Ocean.

Despite the mismatch of our simulated early Eocene climate with reconstructions in the high latitudes, the simulation fulfils our demands for a warm ice-free climate. At the end of the DE_d simulation, the global mean temperature is 7.1 K higher than at the end of the pre-industrial DP_d simulation. The temperature difference is most pronounced in the high latitudes where the DE_d climate is warmer than the DP_d climate by 34.5 K south of 70° S and 10.3 K north of 70° N. In the tropics, the temperature difference is 5.4 K, leading to a weaker pole-to-equator temperature gradient in the DE_d climate than in the DP_d climate. With above-freezing temperatures during most of the year even in the high latitudes, permanent ice is absent and sea ice occurs only seasonally in the Arctic Ocean. The hydrological cycle is enhanced in the DE_d climate, with 15 % stronger precipitation than in the DP_d climate.

In the warm and humid Eocene-like climate, MPI-ESM simulates a dense vegetation cover which matches vegetation reconstructions in the high latitudes (Fig. 2). Like the flora fossil assemblage by Utescher and Mosbrugger (2007)

suggests, extra-tropical trees cover Antarctica and reach the Arctic Ocean in the high north at the end of the DE_d simulation. Beside trees, our model simulates plenty of C$_3$ grass in the mid- to high latitudes. The grass cover disagrees with reconstruction because widespread grassland likely evolved after the early Eocene – between the late Eocene (Bouchenak-Khelladi et al., 2010) and the early to mid-Miocene (20–10 Ma) (Janis, 1993). C$_3$ grass is a common PFT in JS-BACH and we decided to use it despite the discrepancy to the Eocene plant taxa. This approach excludes the influence of characteristic Eocene plant taxa on the stability of the climate–vegetation system and reveals the sensitivity of the stability to geophysical boundary conditions (continents, bathymetry, and atmospheric CO$_2$).

Tropical forest is confined to between 30° S and 30° N in the DE_d simulation, but reconstructions suggest a poleward extent up to 60° S and 60° N during the early Eocene (Fig. 2) (Wolfe, 1985; Willis and McElwain, 2002; Utescher and Mosbrugger, 2007). We assume that the mismatch results from the cold bias in the simulated high-latitude temperature discussed above. C$_4$ grass coexists with tropical forest in the tropics in the DE_d simulation, but the C$_4$ pathway evolved and expanded during the late Miocene (Cerling et al., 1993). Like for C$_3$ grass, we decided to use C$_4$ grass to limit the difference between the Eocene simulations and the pre-industrial simulations to differences in continents, bathymetry, and atmospheric CO$_2$.

In general, deserts are suggested to have been rare in the warm climate of the early Eocene (Willis and McElwain, 2002). Only in central Asia do sediments and flora fossils indicate semi-dry to dry conditions with desert vegetation (Wang et al., 2013; Quan et al., 2012). Like previous simulations by Huber and Caballero (2011) and Loptson et al. (2014), our simulation reproduces the Asian desert because a monsoon climate causes a seasonally dry climate in this region. In subtropical Africa and America, further small deserts and semi-deserts evolve in the DE_d simulation.

4   Results and Discussion

4.1   Bistable deserts in the Eocene climate

The warm and humid early Eocene climate favours a dense vegetation cover in almost all regions. Only in central Asia and in southern Africa do deserts remain in the DE_d simulation (Fig. 2), and subtropical semi-deserts establish themselves in South America, North America, and Australia. In these arid and semi-arid regions, pronounced differences in vegetation cover emerge between the DE_d simulation and the FE_d simulation (Fig. 3).

The difference in the vegetation cover is most pronounced in the Asian desert (region marked in Fig. 3). At the southern edge of the desert, more grass and trees remain in the FE_d simulation than in the DE_d simulation because precipitation is stronger. At the end of the FE_d simulation, precipitation
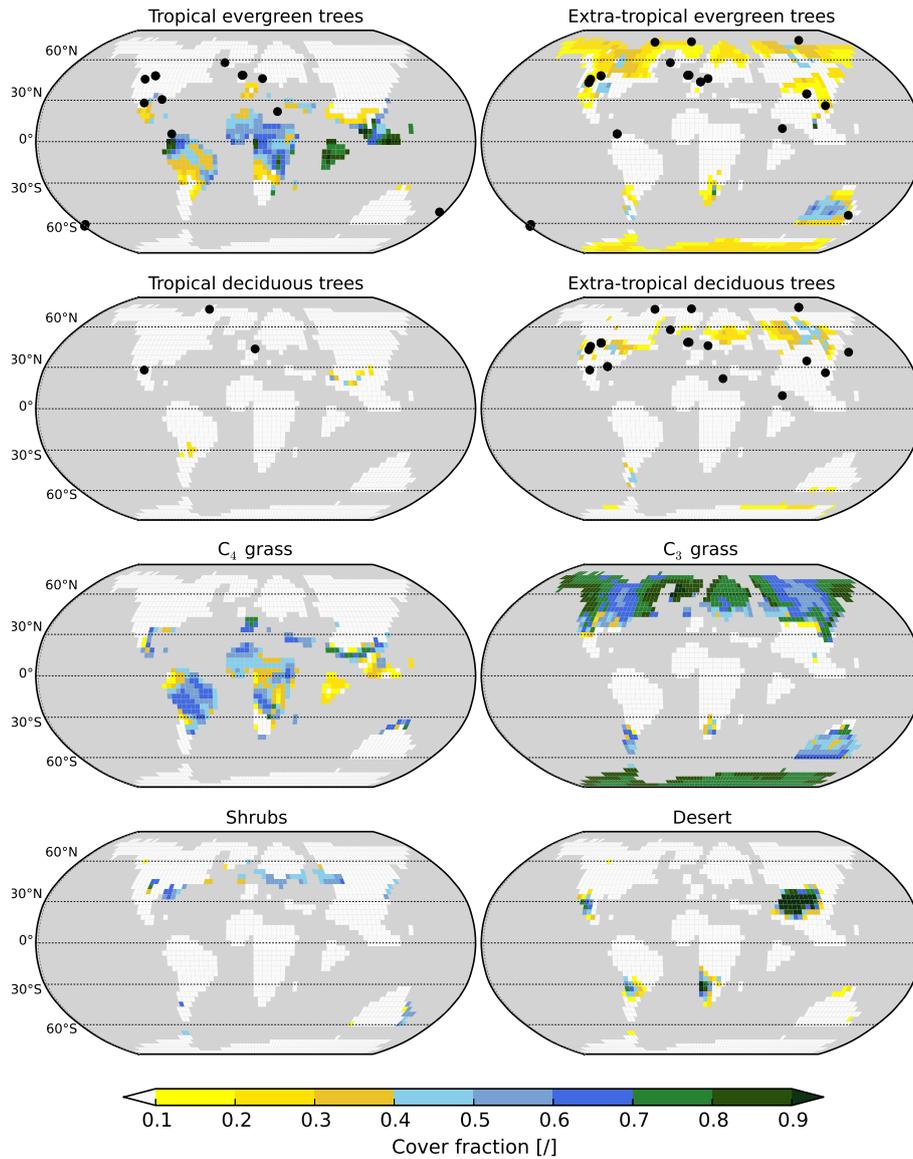
Figure 2. Simulated vegetation cover in the DE_d simulation and reconstructed vegetation based on the flora collection by Utescher and Mosbrugger (2007). Locations where the diversity of the respective PFT in flora collection exceeds 10 % are marked.

in central Asia is 1.58 mm day^{-1} stronger and desert cover is 0.36 smaller (Fig. 4a). In the semi-desert in southern Africa, desert cover is also smaller at the end of the FE_d simulation than at the end of the DE_d simulation (Fig. 4d).

In the semi-desert in western North America, precipitation is smaller by 0.52 mm day^{-1} (70 %) at the end of the FE_d simulation than at the end of the DE_d simulation. In the drier climate, desert cover is larger by 0.43 mm day^{-1} (Fig. 4c). In the semi-desert in southern South America, a weaker precipitation in the FE_d simulation also results in a larger desert cover than in the DE_d simulation (Fig. 4b). The differences on the American continents are counterintuitive because starting from dense forest leads to a larger desert in these regions than starting from bare soil. This result dis-

agrees with all simulations mentioned in the introduction. Later, we will discuss the mechanism causing these bistabilities.

To identify the driving mechanisms for the multiple steady vegetation states, we analyse the large-scale atmospheric circulation. Following Claussen (1997), we compute the velocity potential at 200 hPa, which is an indicator of large-scale upper-air divergence and convergence and, hence, convection and subsidence in the tropics. The separation of the horizontal wind, $\mathbf{V}$, into the rotational component, $\mathbf{V}_\Psi$, and the divergent component, $\mathbf{V}_\chi$, yields

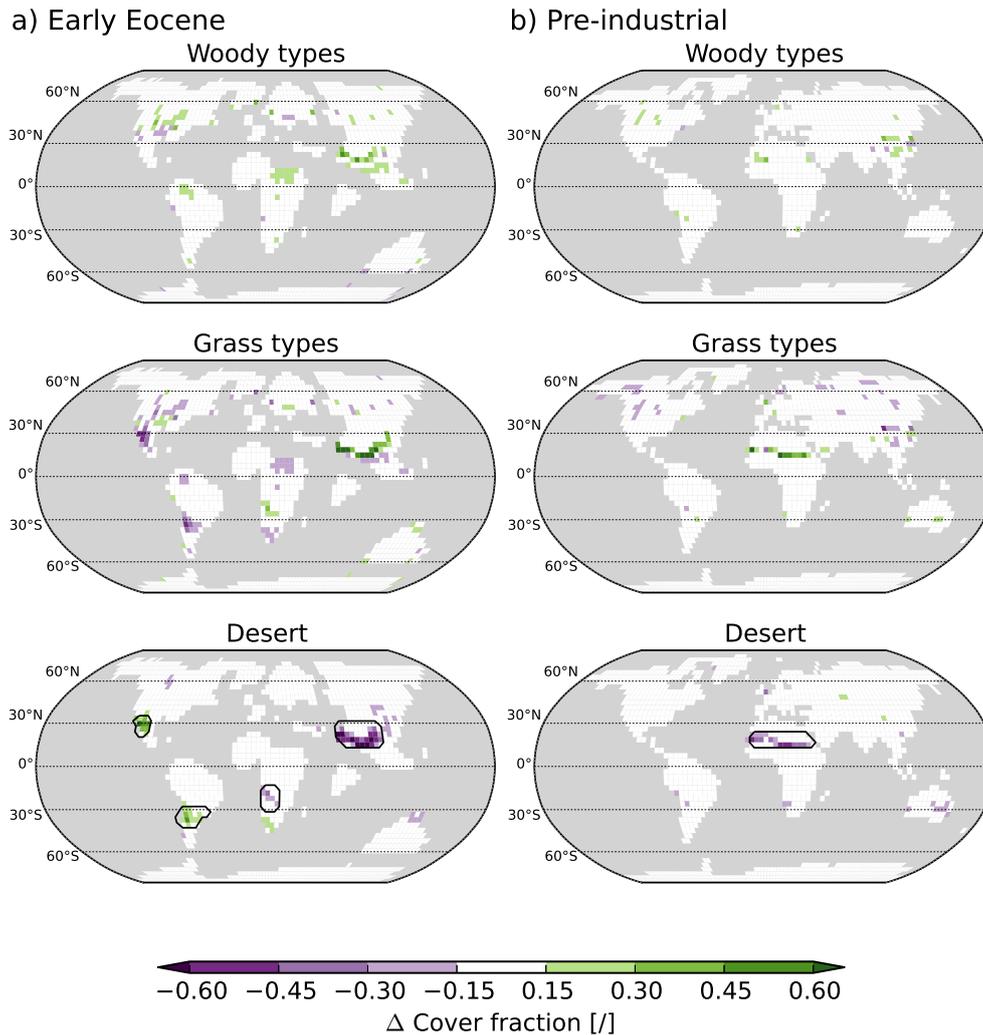$$\mathbf{V} = \mathbf{V}_\Psi + \mathbf{V}_\chi. \tag{1}$$

Figure 3. Differences in vegetation cover between the simulations that start from a forest world and the simulations that start from a desert world. Differences for the early Eocene climate (FE$_d$–DE$_d$) **(a)** and for the pre-industrial climate (FP$_d$–DP$_d$) **(b)** are shown. Mapped differences refer to the average over 30 years and are significant on a 95 % level. Woody types include all trees and shrubs. Grass types refer to C$_4$ grass and to C$_3$ grass. Black contour lines mark regions which are analysed in more detail in Figs. 4 and 9.

The divergent part of the horizontal wind is the gradient of the velocity potential, χ,

$$\nabla \chi = \mathbf{V}_\chi. \tag{2}$$

Hence, the divergent part of the large-scale horizontal wind is directed towards the strongest increase in the velocity potential. This relation implies that air flows from the centre of negative velocity potential to the centre of positive velocity potential. Therefore, upper air diverges in the centre of negative velocity potential and converges in the centre of positive velocity potential. Below the divergence, air rises, and below the convergence, air subsides.

Figure 5 shows the velocity potential in the desert world, DE$_f$, and in the forest world, FE$_f$, at 200 hPa averaged over the last 30 years of the simulations. In the desert world, the centre of positive velocity potential indicates strong subsi-

dence over the tropical Atlantic Ocean, and the centre of negative velocity potential implies convection over the tropical Pacific Ocean (Fig. 5a). In the forest world, the centre of subsidence intensifies and shifts to northern South America relative to the circulation in the desert world, and the centre of convection intensifies and shifts to the western Pacific Ocean (Fig. 5b).

Starting from the desert world simulation and the forest world simulation, vegetation cover evolves dynamically with climate during the DE$_d$ simulation and the FE$_d$ simulation, respectively. The initial large-scale atmospheric circulation pattern, however, persists (Fig. 5c, d). Hence, at the end of the simulations, the atmospheric circulation still differs strongly between the DE$_d$ simulation and the FE$_d$ simulation. With stronger convection over the west Pacific Ocean in the FE$_d$ simulation, precipitation at the southern edge of the Asian
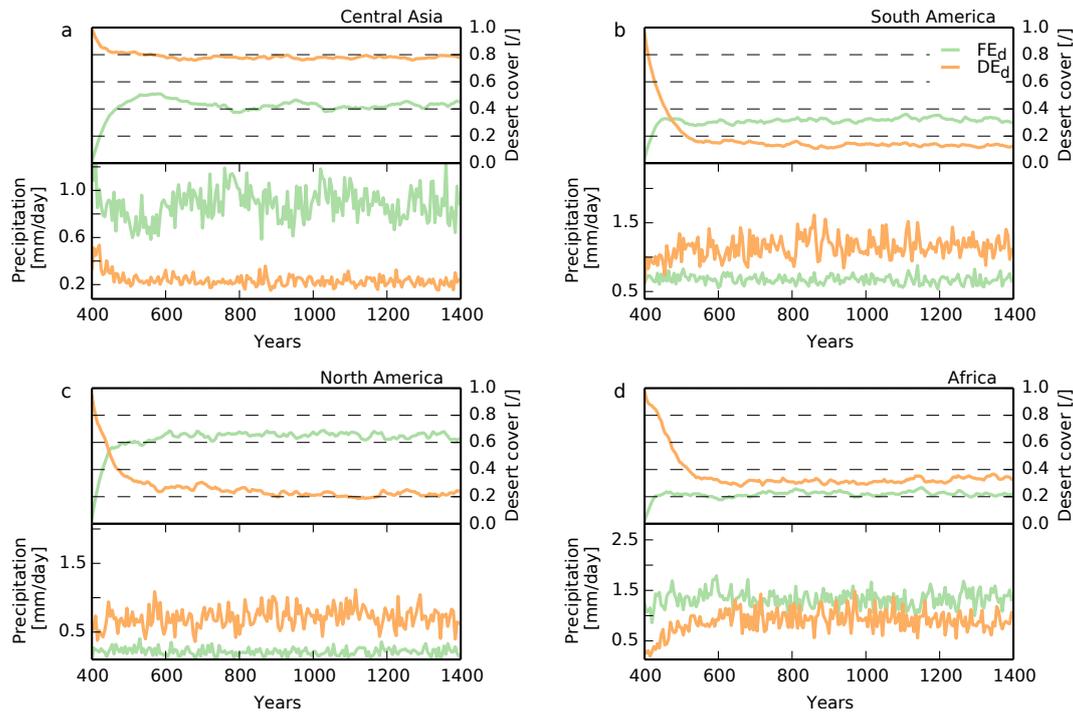
Figure 4. Time series of 5-year mean desert cover and precipitation in selected regions in central Asia (**a**), South America (**b**), North America (**c**), and Africa (**d**) in the FE_d simulation (green line) and in the DE_d simulation (orange line). The regions are marked in Fig. 3.
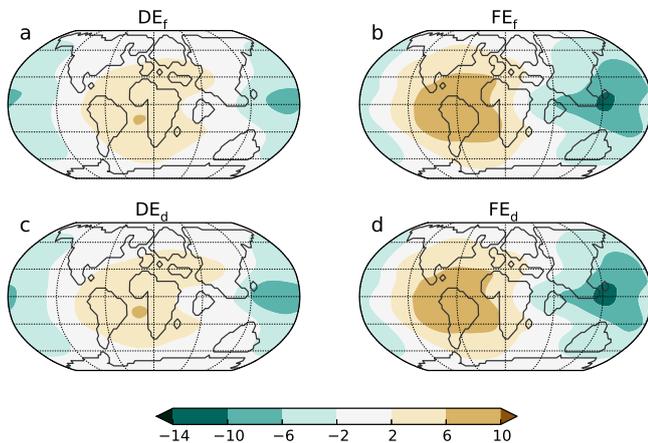

Figure 5. Velocity potential at 200 hPa at the end of the desert world simulation (**a**), forest world simulation (**b**), DE_d simulation (**c**), and FE_d simulation (**d**). The average over the last 30 years of each simulation is considered. The DE_d simulation and the FE_d simulation start from the desert world simulation and the forest world simulation, respectively. Brown colours indicate to a positive velocity potential, upper-air convergence, and subsidence. Green colours indicate to a negative velocity potential, upper-air divergence, and rising.

desert is stronger than in the DE_d simulation, leading to a smaller desert cover. Over the American continents, where subsidence strengthens relative to the DE_d simulation, the

subtropical semi-arid regions are drier and desert cover is larger.

In the desert world, a temperature gradient occurs above 100 hPa between cold air above the tropics and warmer air above the mid- and high latitudes (Fig. 7). This meridional temperature gradient induces a weak easterly wind at about 5° N due to the thermal wind relation (Fig. 7). In the forest world, near-surface temperature is reduced relative to the desert world, and in the colder climate, the tropopause is lower, leading to a warming at the tropopause. The tropopause decline and the connected warming reach 200 hPa in the mid- and high latitudes and 100 hPa in the tropics. Due to the weaker warming in the tropics than in the mid- to high latitudes, the meridional temperature gradient between tropics and mid- to high latitudes enhances relative to the desert world. With a stronger meridional temperature gradient, the easterly wind at 100 hPa strengthens in the forest world.

The stronger easterly wind in the forest world transports more air from the convection zone over Asia to the subsidence zone over America than in the desert world. The enhanced air transport manifests itself in an intensified velocity potential pattern and a general westward shift relative to the desert world (Fig. 5). This result suggests that forest affects large-scale atmospheric circulation by reducing near-surface temperature and lowering tropopause height, thereby, enhancing the easterly wind at the tropopause.
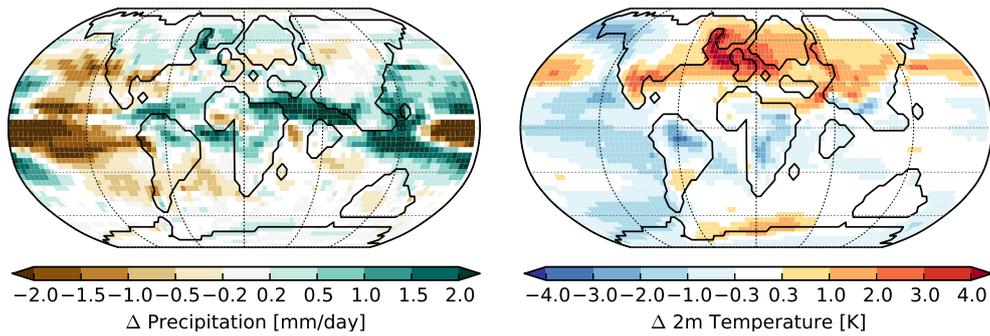
Figure 6. Differences in precipitation and 2 m temperature between the FE$_d$ simulation and the DE$_d$ simulation. The average over the last 30 years of the simulations is considered. Depicted differences are significant on a 95 % level.
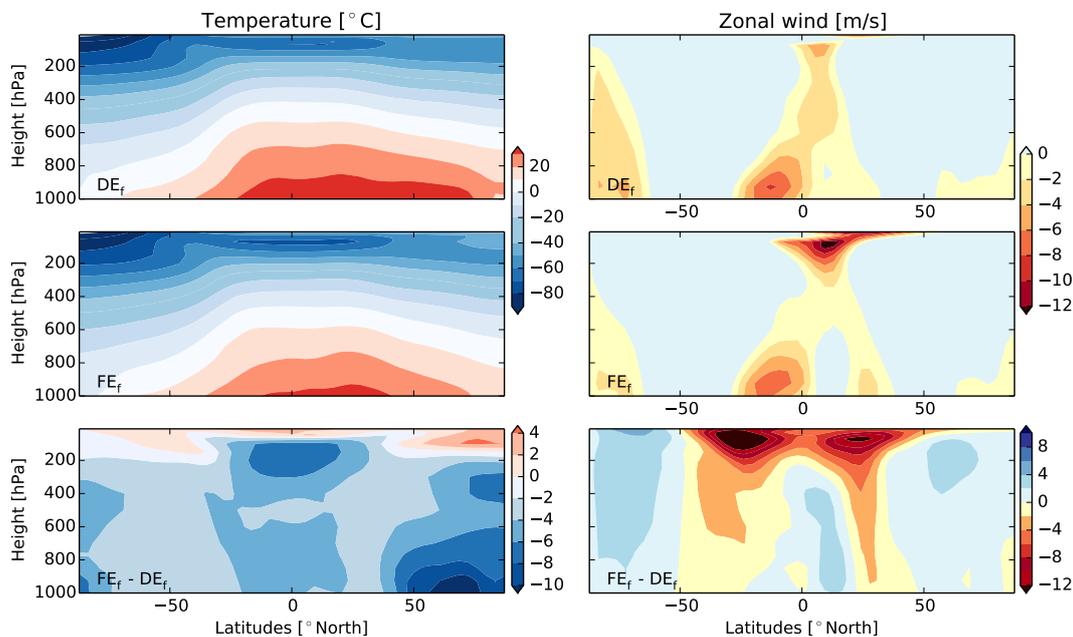

Figure 7. Zonal-mean temperature and wind in the desert world simulation, DE$_f$, and in the forest world, FE$_f$, simulation of the early Eocene climate. Moreover, the differences between the forest world simulation and the desert world simulation (FE$_f$–DE$_f$) is shown. The average of July and August in the last 30 years of the simulations is considered.

During the FE$_d$ simulation, the warming in the height becomes weaker but the easterly wind is still stronger than in the DE$_d$ simulation and supports the intensified and shifted velocity potential pattern (not shown here). The persistence of the stronger easterly wind in the FE$_d$ simulation again indicates that the initial forest cover shifts the atmospheric circulation to a self-preserving state other than the desert cover.

To test whether large-scale or local initial vegetation causes the bistability in the climate–vegetation system, we perform two additional simulations. In the Asian desert simulation, DA$_f$, we fix the vegetation cover to a desert in central Asia (region highlighted in Fig. 8) and to forests elsewhere and simulate 400 years. After that, we let the vegetation evolve dynamically during the DA$_d$ simulation. Analogously, we assume a dense forest in central Asia and deserts else-

where in the Asian forest simulation, FA$_f$. After 400 years with a fixed vegetation cover, vegetation evolves dynamically in the FA$_d$ simulation.

In the DA$_f$ simulation, when vegetation is fixed, the atmospheric circulation reaches the same state as in the forest world. Then, vegetation evolves dynamically and the circulation pattern persists ending up in the same stable state as in the FE$_d$ simulation. Analogously, the FA$_f$ simulation yields the same large-scale atmospheric circulation as the desert world simulation. With a dynamically evolving vegetation cover, the atmospheric circulation persists leading to the same state in the FA$_d$ simulation as in the DE$_d$ simulation. The agreement of the DA$_d$ simulation with the FE$_d$ simulation and the FA$_d$ simulation with the DE$_d$ simulation shows that local initial vegetation fails to cause multiple climate–
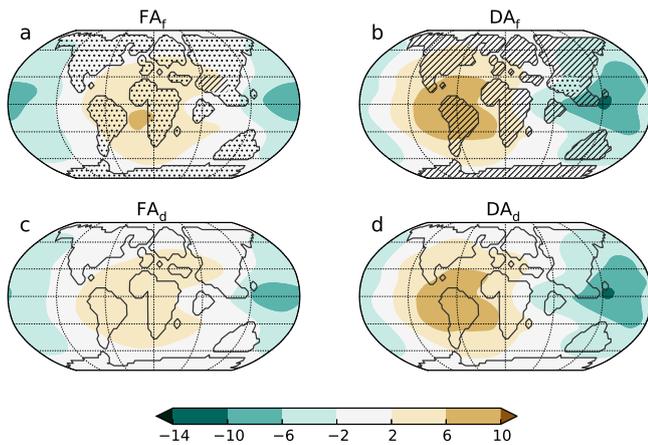
Figure 8. Velocity potential at 200 hPa at the end of the FA$_f$ simulation and DA$_f$ simulation **(a–b)** and at the end of the FA$_d$ simulation and DA$_d$ simulation **(c–d)**. The average over the last 30 years of each simulation is considered. Brown colours indicate to a positive velocity potential, upper-air convergence, and subsidence. Green colours indicate to a negative velocity potential, upper-air divergence, and rising.

vegetation states. Instead, our results suggest that large-scale initial vegetation cover causes multiple climate–vegetation states in the warm, ice-free climate.

4.2 Bistable Sahel in the pre-industrial climate

In the pre-industrial climate, the vegetation difference between the FP$_d$ simulation and the DP$_d$ simulation is restricted to the Sahel. More vegetation remains in this region and the desert cover is smaller by 0.21 in the FP$_d$ simulation than in the DP$_d$ simulation. Consistently, precipitation is about 2 times larger in the FP$_d$ simulation than in the DP$_d$ simulation (Fig. 11).

In contrast to the Eocene simulations, the large-scale atmospheric circulation, as indicated by the 200 hPa velocity potential, differs only slightly between the forest world simulation and the desert world simulation for pre-industrial climate (Fig. 10a, b). When vegetation is allowed to dynamically adjust to and to interact with climate, the small differences in the large-scale atmospheric circulation between the initially forested world and the initially bare world nearly vanish (Fig. 10c, d). The weak impact of initial vegetation on the large-scale atmospheric circulation implies that a local effect rather than a large-scale effect leads to multiple climate–vegetation states in the pre-industrial Sahel climate.

In the Sahel, evapotranspiration amounts to 1.1 mm day^{-1} in the FP$_d$ simulation and 0.64 mm day^{-1} in the DP$_d$ simulation. Cloud cover is larger, less solar radiation reaches the surface, and latent heat flux is larger by a factor of 1.7 in the FP$_d$ simulation than in the DP$_d$ simulation. Consistently, a stronger meridional temperature gradient develops with warmer air over the Sahara and colder air over the Sahel in
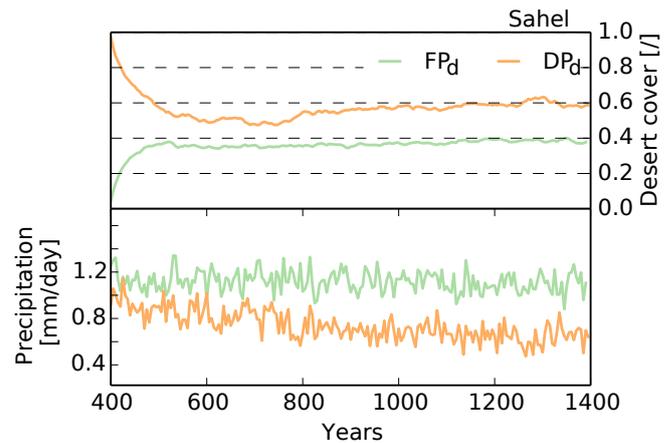

Figure 9. Time series of 5-year mean desert cover and precipitation in the pre-industrial Sahel in the FP$_d$ simulation (green line) and in the DP$_d$ simulation (orange line). The Sahel region is marked in Fig. 3.
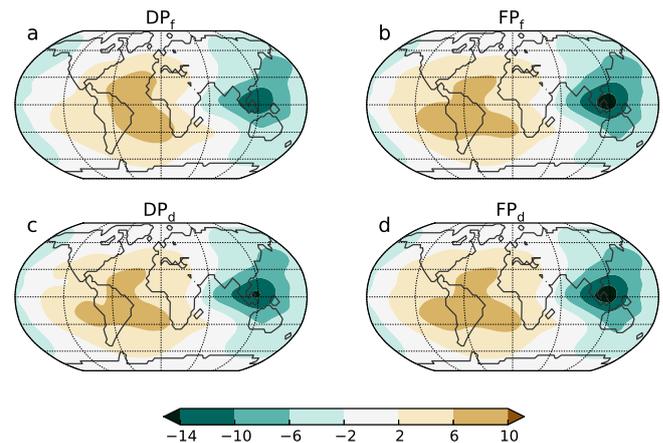

Figure 10. Velocity potential at 200 hPa at the end of the desert world simulation **(a)**, the forest world simulation **(b)**, the DP$_d$ simulation **(c)**, and the FP$_d$ simulation **(d)**. The average over the last 30 years of the respective simulation is considered. The DP$_d$ simulation and the FP$_d$ simulation start from the desert world simulation and the forest world simulation, respectively. Brown colours indicate to a positive velocity potential, upper-air convergence, and subsidence. Green colours indicate to a negative velocity potential, upper-air divergence, and rising.

the FP$_d$ simulation than in the DP$_d$ simulation (Fig. 11). The increased temperature gradient enhances the African easterly jet (AEJ) at 700 hPa in the FP$_d$ simulation (Fig. 12). Stronger AEJ over the moister or greener Sahel region is in line with earlier simulations by Cook (1999) and Rachmayani et al. (2015). The stronger AEJ is accompanied by a stronger horizontal moisture flux convergence (Fig. 12) which, in turn, leads to larger precipitation over the Sahel in the FP$_d$ simulation than in the DPd simulation (Fig. 11).
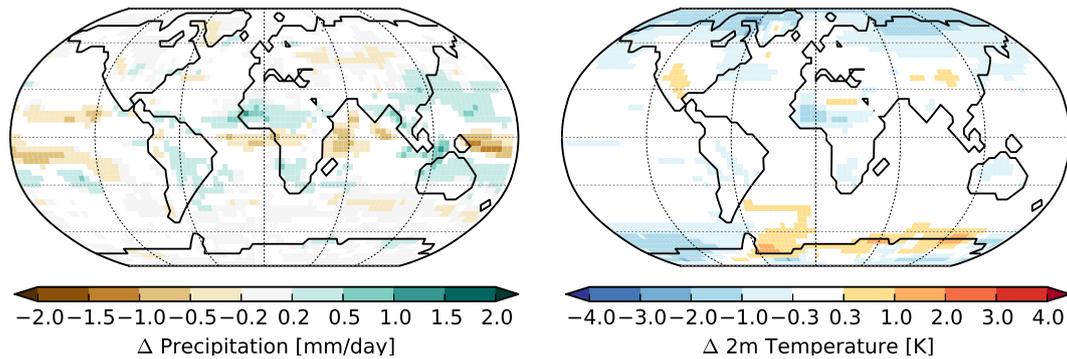
Figure 11. Differences in precipitation and 2 m temperature between the end of the FD$_P$ simulation and the end of the DD$_P$ simulation. Depicted differences are significant on a 95 % level.
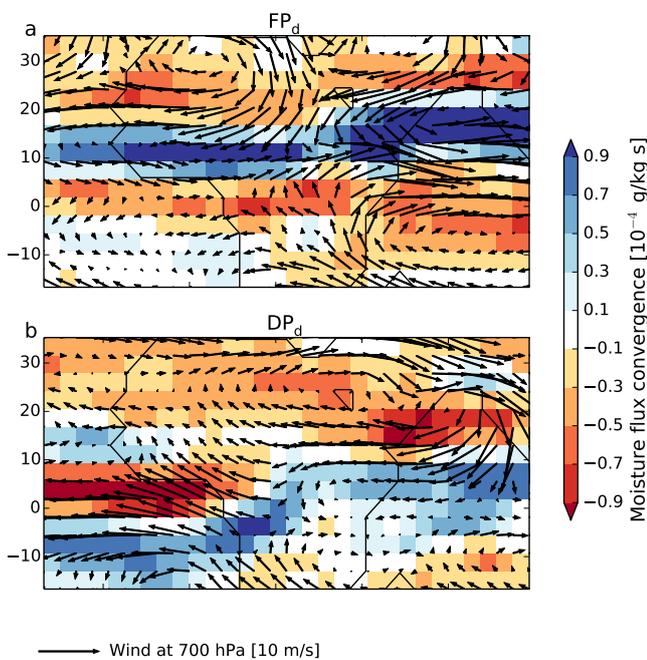

Figure 12. Horizontal wind at 700 hPa averaged over July, August, and September in the last 30 years of the FP$_d$ simulation and DE$_d$ simulation. Colours show the moisture flux convergence.

In the studies by Claussen and Gayler (1997) and Claussen (1998), strong differences in surface albedo triggered multiple stable vegetation–atmosphere states in the Sahara and Sahel. In our study, albedo differences are assumed to be small. Hence, a hydrological feedback causes multiple states, as is the case in the simulations by Rachmayani et al. (2015).

5 Conclusions

To our knowledge, the transitivity of the global climate–vegetation system has so far only been explored for late Quaternary climate, i.e. glacial, interglacial mid-Holocene, and present-day climate. Therefore, we extend the analysis

to early Eocene conditions, i.e. to a warm, almost ice-free climate with a different configuration of continents than today. To this end, we initialize the simulations by prescribing either dense forests or bare deserts on all continents both for early Eocene and pre-industrial climate. For early Eocene conditions, multiple equilibrium states evolve: starting with desert continents, an extended desert remains in central Asia; starting with complete forest cover, the Asian desert is much smaller, while coastal deserts develop in the Americas which appear to be larger than in the simulations with initially bare continents. We attribute these differences to differences in the large-scale atmospheric circulation. With initially forested continents, a stronger dipole in the 200 hPa velocity potential develops than in the simulation with initially bare continents. This difference prevails when vegetation is allowed to interact with climate.

Additional simulations with initial surface conditions that differ in the region of the Asian desert only indicate that local feedback processes are less important for the development of multiple states. Initializing a simulation with a patch of Asian desert in an otherwise completely forested world leads to mainly the same equilibrium as when the simulation is initialized with completely forested continents. The same is valid if a patch of Asian forest is prescribed in simulations with initially bare continents. It would be interesting to find the spatial extent of the initial perturbation, or the repeller, over the Asian continent from which the system is driven into different modes.

In the pre-industrial climate, local vegetation–precipitation feedbacks seem to cause multiple equilibrium climate–vegetation states which are restricted to the Sahel region. In the simulations with large-scale initial forest cover, forests cool the Sahel in comparison with the simulations with initially bare continents. This cooling is associated with stronger latent heat flux and stronger cloud cover. The difference in local cooling results in a stronger meridional temperature gradient between cold air above the Sahel and warmer air above the Sahara. The difference in the meridional temperature contrast, in turn, fuels the African

easterly jet which transports moisture to the Sahel and thereby supports vegetation growth in the simulation with initially forested continents. Hence, in these simulations, and in line with previous studies (e.g. Rachmayani et al., 2015), it is a local hydrological climate–vegetation feedback which leads to multiple equilibria over the Sahel region in the pre-industrial climate.

In our study, we focused on biogeophysical processes and associated intransitivity of the climate–vegetation system. We neglected any differences between plant taxa and used pre-industrial PFTs for the early Eocene climate simulation. The strongest discrepancy between Eocene plant taxa and the PFTs used concerns grasses. JSBACH considers C_3 grass and C_4, but C_3 grasses occurred rarely during the early Eocene and C_4 grasses did not exist at all. To solve this discrepancy, one might exclude C_4 grasses and replace C_3 grasses by fern and herbs which grew plentifully during that time (Utescher and Mosbrugger, 2007). Assuming fern and herbs instead of C_3 grass, we expect that fern and herbs would spread in the region where we have simulated C_3 grass before because JSBACH only distinguishes between woody vegetation, i.e. trees and shrubs, and non-woody vegetation, i.e. every species except trees and shrubs. Presumably, JSBACH would handle fern and herbs in the same way as it handles grass. By allowing fern and herbs to grow in tropical temperatures, we assume that fern and shrubs would also capture the niche of C_4 grass.

References

Bathiany, S., Claussen, M., , and Fraedrich, K.: Implications of climate variability for the detection of multiple equilibria and for rapid transitions in the atmosphere-vegetation system, Clim. Dynam., 38, 1775–1790, 2012.

Bathiany, S., Claussen, M., and Fraedrich, K. F.: Detecting hotspots of atmosphere-vegetation interaction via slowing down – Part 1: A stochastic approach, Earth Syst. Dynam., 4, 63–78, doi:10.5194/esd-4-63-2013, 2013a.

Bathiany, S., Claussen, M., and K. Fraedrich, K.: Detecting hotspots of atmosphere-vegetation interaction via slowing down – Part 2:

Application to a global climate model, Earth Syst. Dynam., 4, 79–93, doi:10.5194/esd-4-79-2013, 2013b.

Beerling, D. and Royer, D.: Convergent Cenozoic CO_2 history, Nat. Geosci., 4, 418–420, 2011.

Bice, K. L. and Marotzke, J.: Numerical evidence against reversed thermohaline circulation in the warm Paleocene/Eocene ocean, J. Geophys. Res., 106, 11529–11542, 2001.

Bijl, P. K.: Early Palaeogene temperature evolution of the southwest Pacific Ocean, Nature, 461, 776–779, 2009.

Bouchenak-Khelladi, Y., Verboom, G. A., Savolainen, V., and Hodkinson, T. R.: Biogeography of the grasses (Poaceae): a phylogenetic approach to reveal evolutionary history in geographical space and geological time, Botan. J. Linn. Soc., 162, 543–557, 2010.

Brovkin, V., Claussen, M., Petoukhov, V., and Ganopolski, A.: On the stability of the atmosphere-vegetation system in the Sahara/Sahel region, J. Geophys. Res.-Atmos., 103, 31613–31624, 1998.

Brovkin, V., Raddatz, T., and Reick, C. H.: Global biogeophysical interactions between forest and climate, Geophys. Res. Lett., 36, L07405, doi:10.1029/2009GL037543, 2009.

Cerling, T., Wang, Y., and Quade, J.: Expansion of C4 ecosystems as an indicator of global ecological change in the late Miocene, Nature, 361, 344–345, 1993.

Claussen, M.: On coupling global biome models with climate models, Clim. Res., 4, 203–221, 1994.

Claussen, M.: Modeling bio-geophysical feedback in the African and Indian monsoon region, Clim. Dynam., 13, 247–257, 1997.

Claussen, M.: On multiple solutions of the atmosphere-vegetation system in present-day climate, Glob. Change Biol., 4, 549–559, 1998.

Claussen, M. and Gayler, V.: The Greening of the Sahara during the Mid-Holocene: Results of an Interactive Atmosphere-Biome Model, Glob. Ecol. Biogeogr. Lett., 6, 369–377, 1997.

Claussen, M., Kubatzki, C., Brovkin, V., Ganopolski, A., Hoelzmann, P., and Pachur, H.-J.: Simulation of an abrupt change in Saharan vegetation in the Mid-Holocene, Geophys. Res. Lett., 26, 2037–2040, 1999.

Cook, K. H.: Generation of the African Easterly Jet and Its Role in Determining West African Precipitation, J. Clim., 12, 1165–1184, 1999.

Dekker, S. C., de Boer, H. J., Brovkin, V., Fraedrich, K., Wassen, M. J., and Rietkerk, M.: Biogeophysical feedbacks trigger shifts in the modelled vegetation-atmosphere system at multiple scales, Biogeosciences, 7, 1237–1245, doi:10.5194/bg-7-1237-2010, 2010.

Eberle, J. J. and Greenwood, D. R.: Life at the top of the greenhouse Eocene world-A review of the Eocene flora and vertebrate fauna from Canada's High Arctic, Geol. Soc. Am. Bull., 124, 3–23, 2012.

Harrington, G. J., Eberle, J., Le-Page, B. A., Dawson, M., and Hutchison, J. H.: Arctic plant diversity in the Early Eocene greenhouse, Proc. Roy. Soc. B, 279, 1515–1521, 2012.

Heinemann, M., Jungclaus, J. H., and Marotzke, J.: Warm Paleocene/Eocene climate as simulated in ECHAM5/MPI-OM, Clim. Past, 5, 785–802, doi:10.5194/cp-5-785-2009, 2009.

Huber, M. and Caballero, R.: The early Eocene equable climate problem revisited, Clim. Past, 7, 603–633, doi:10.5194/cp-7-603-2011, 2011.

Ilyina, T., Six, K. D., Segschneider, J., Maier-Reimer, E., Li, H., and Nunez-Riboni, I.: Global ocean biogeochemistry model HAMOCC: Model architecture and performance as component of the MPI-Earth System Model in different CMIP5 experimental realizations., J. Adv. Model. Earth Syst., 5, 287–315, 2013.

Janis, C. M.: Tertiary mammal evolution in the context of changing climates, vegetation, and tectonic events, Ann. Rev. Ecol. Syst., 24, 467–500, 1993.

Jungclaus, J. H., Fischer, N., Haak, H., Lohmann, K., Marotzke, J., Matei, D., Mikolajewicz, U., Notz, D., and von Storch, J. S.: Characteristics of the ocean simulations in the Max Planck Institute Ocean Model (MPIOM) the ocean component of the MPI-Earth system model, J. Adv. Model. Earth Syst., 5, 422–446, 2013.

Kubatzki, C. and Claussen, M.: Simulation of the global bio-geophysical interactions during the Last Glacial Maximum, Clim. Dynam., 14, 461–471, 1998.

Loptson, C. A., Lunt, D. J., and Francis, J. E.: Investigating vegetation-climate feedbacks during the early Eocene, Clim. Past, 10, 419–436, doi:10.5194/cp-10-419-2014, 2014.

Lorenz, E.: Climatic Determinism, Meteor. Monogr., 8, 1–3, 1968.

Lunt, D. J., Jones, T., Heinemann, M., Huber, M., LeGrande, A., Winguth, A., Loptson, C., Marotzke, J., Roberts, C. D., Tindall, J., Valdes, P., and Winguth, C.: A model-data comparison for a multi-model ensemble of early Eocene atmosphere-ocean simulations: EoMIP, Clim. Past, 8, 1717–1736, doi:10.5194/cp-8-1717-2012, 2012.

Oyama, M. D. and Nobre, C. A.: A new climate-vegetation equilibrium state for tropical South America, Geophys. Res. Lett., 30, 2199, doi:10.1029/2003GL018600, 2003.

Pearson, P., van Dongen, B., Nicholas, C., Pancost, R., and Schouten, S.: Stable warm tropical climate through the Eocene Epoch, Geology, 35, 211–214, 2007.

Pross, J., Contreras, L., Bijl, P. K., Greenwood, D. R., Bohaty, S. M., Schouten, S., Bendle, J. A., Röhl, U., Tauxe, L., Ian Raine, J., Huck, C. E., van de Flierdt, T., Jamieson, S. S. R., Stickley, C. E., van de Schootbrugge, B., Escutia, C., Brinkhuis, H., and Program, I. O. D.: Persistent near-tropical warmth on the Antarctic continent during the early Eocene epoch, Nature, 488, 73–77, 2012.

Quan, C., Liu, Y., and Utescher, T.: Eocene monsoon prevalence over China: A paleobotanical perspective, Palaeogeogr. Palaeoclimatol. Palaeoecol., 365, 302–311, 2012.

Rachmayani, R., Prange, M., and Schulz, M.: North African vegetation-precipitation feedback in early and mid-Holocene climate simulations with CCSM3-DGVM, Clim. Past, 11, 175–185, doi:10.5194/cp-11-175-2015, 2015.

Reick, C. H., Raddatz, T., Brovkin, V., and Gayler, V.: Representation of natural and anthropogenic land cover change in MPI-ESM, J. Adv. Model. Earth Syst., 5, 459–482, 2013.

Renssen, H., Goosse, H., and Fichefet, T.: On the non-linear response of the ocean thermohaline circulation to global deforestation, Geophys. Res. Lett., 30, 1061, doi:10.1029/2002GL016155, 2003.

Sluijs, A., Schouten, S., Pagani, M., Woltering, M., Brinkhuis, H., Sinninghe Damste, J. S., Dickens, G. R., Huber, M., Reichart, G., Stein, R., Matthiessen, J., Lourens, L. J., Pedentchouk, N., Backman, J., Moran, K., and the Expedition 302 Scientists: Subtropical Arctic Ocean temperatures during the Palaeocene/Eocene thermal maximum, Nature, 441, 610–613, 2006.

Stevens, B., Giorgetta, M., Esch, M., Mauritsen, T., Crueger, T., Rast, S., Salzmann, M., Schmidt, H., Bader, J., Block, K., Brokopf, R., Fast, I., Kinne, S., Kornblueh, L., Lohmann, U., Pincus, R., Reichler, T., and Roeckner, E.: Atmospheric component of the MPI-M Earth System Model: ECHAM6, J. Adv. Model. Earth Syst., 5, 146–172, 2013.

Utescher, T. and Mosbrugger, V.: Eocene vegetation patterns reconstructed from plant diversity – A global perspective, Palaeogeogr. Palaeoclimatol. Palaeoecol., 247, 243–271, 2007.

Wang, D., Lu, S., Han, S., Sun, X., and Quan, C.: Eocene prevalence of monsoon-like climate over eastern China reflected by hydrological dynamics, J. Asian Earth Sci., 62, 776–787, 2013.

Wang, G. and Eltahir, E.: Biosphere-atmosphere interactions over West Africa. II: Multiple climate equilibria, Quarterly J. Roy. Meteorol. Soc., 126, 1261–1280, 2000.

Willis, K. and McElwain, J.: The elvolution of plants, Oxford University Press, USA, 2002.

Wolfe, J.: Distribution of major vegetation types during the Tertiary, in: The carbon cycle and atmospheric CO_2: natural variations Archean to present, edited by: Sundquist E. T. and Broecker W. S., American Geophysical Union, Washington/DC, 357–375, 1985.

Zachos, J., Berza, J., and Wise, S.: Early Oligocene ice-sheet expansion on Antarctica – Stable isotope and sedimentological evidence from Kerguelen Plateau southern Indian-Ocean, Geology, 20, 569–573, 1992.

Zachos, J., Pagani, M., Sloan, L., Thomas, E., and Billups, K.: Trends, rhythms, and aberrations in global climate 65 Ma to present, Science, 292, 686–693, 2001.

Zeng, N. and Neelin, D. J.: The role of vegetation-climate interaction and interannual variability in shaping the African savanna, J. Climate, 13, 2665–2670, 2000.